Chapter 2

Ultracold Atom Production

This chapter describes the critical elements and functionality of the laser cooling apparatus which produces and delivers cold atomic ensembles to the mm-scale magnetic trap which is described in the next chapter. As ultracold atom experiments have proliferated over the last decade, much of the basic infrastructure has become very established technology. The aim of this section is to lay out the specific design considerations and peculiarities of our apparatus with the theoretical background behind each subsystem referenced to the giants upon whose shoulders we stood when constructing the apparatus.

Ultracold atom production is built upon a number of integrated primary physical elements. Crucial systems found in these experiments include:

Ultra-high vacuum (UHV) chamber - This must be able to achieve pressures $\leq 10^{-10}$ torr and accommodate all necessary experimental elements (e.g. atomic sources, optical access, electronic control).

Bright atom source - This must provide a sufficiently high-flux source of atoms to be laser-cooled.

Frequency-locked laser system - These lasers must have sufficient coherence (linewidth $\leq$ MHz), tunability, and power to laser-cool a large atom population. Also included in this system are the various optics and optical control elements necessary to cool, address, and image a cloud of atoms.

Atom trapping - This can be either an optical trapping system or a magnetic trap-

ping system.

Electronic control - Because of the immense complexity and time-ordered sequencing of ultracold atomic experiments, substantial electronic infrastructure is required to operate the myriad control elements, e.g. beam shutters, acousto-optic modulators (AOMs), power supplies, etc.[1]

Imaging system - This optical probe is the main diagnostic and data collection system, allowing interrogation of the atomic ensemble.

The description of these systems and their performance will occupy the bulk of this chapter. The underlying physics of manipulating atoms with external electromagnetic fields that makes this work possible is well described elsewhere [20, 57].

2.1 The UHV Chamber

That a floating cloud of gas $1/10,000$th the density of air can achieve nK temperatures while surrounded by a 300 K steel vacuum chamber is at least counterintuitive, if not magical. The reason this is possible is the extremely low pressures achievable with modern vacuum technology, providing the requisite insulation from heating or loss due to collisions between the ultracold gas and 300 K background molecules. Reaching the UHV regime of pressure ($\lesssim 10^{-9}$ torr) is an absolute requirement for ultracold atomic physics experiments, and $< 10^{-10}$ torr is usually needed for most experiments.

The vacuum chamber in which this work was carried out accommodates a "loading region" where the cold atoms would be collected in a magneto-optical trap (MOT) and the "millitrap/cavity region" to which the atom population would be subsequently transported. As the optical beams which form the MOT are roughly 1" in diameter, this set a separation scale between these regions on the order of a few inches. The rationale behind the decision to incorporate both regions in the same steel chamber is one of simplicity, where only two magnetic trapping coils (described later in this chapter) are required to effect the displacement from loading to the science region.

The main pumping elements are a 110 L/s ion pump (Thermionics TP-110) and two

[1] This is included for completeness, but as the computer control system used for this work was designed and programmed by Dan Stamper-Kurn while he was at MIT [21] and implemented on this experiment by Tom Purdy, it will not be outlined in this thesis.

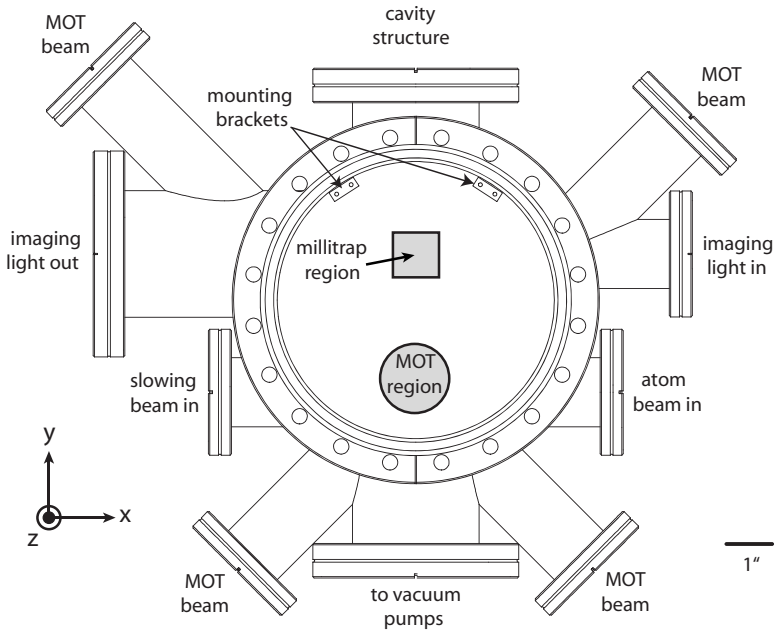

Figure 2.1: Sketch of the main chamber with the two focii of the system. The vacuum ports are labeled by primary function.

titanium sublimation (Ti:sub) pumps. The primary Ti:sub pump is surrounded by a "shroud" (Thermionics SS400/275) which is cooled by liquid nitrogen during experimental operation, increasing the pumping speed. The secondary Ti:sub pump is mounted on a retractable vacuum piece (Thermionics LMA-8) along the "slowing beam" arm of the main chamber. This allows the deposition of titanium on the interior of the main chamber and along the slower tube. With a standard bakeout [58], the system reached the final pressures shown in Table 2.1.

2.2 Optical System

In addition to the simple hydrogen-like atomic structure and collisional properties which make it a good atom for evaporative cooling [59, 60], the major selling point for using rubidium in laser-cooling experiments is the relative ease with which the necessary laser light is produced with external cavity diode laser (ECDL) systems [61]. By the time the work presented in the last two chapters of this thesis commenced, no less than six

Integrated	Final Pressure
millitrap only (Ch. 3-5), room temp	3×10^{-11} torr
millitrap only (Ch. 3-5), lN_2 flowing	2×10^{-11} torr
millitrap and cavity (Ch. 6), room temp	7×10^{-11} torr
millitrap and cavity (Ch. 6), lN_2 flowing	5×10^{-11} torr

Table 2.1: Final experimental pressures. The relatively higher pressure after the cavity installation (discussed in chapter 6) is likely due to extra outgassing from the some of the construction materials used in the mounting structure, e.g. Viton, Teflon, piezoelectric ceramics, and the cavity mirrors. These pressures were measured with an ion gauge that was relatively far from the main chamber and very close to the vacuum pumps. While the values are probably best considered lower bounds, the vacuum-limited lifetime of the atoms did roughly conform to these pressures.

distinct diode laser systems (three commercial, three home-built) were actively used in the experimental cycle. Four of these were used entirely for laser-cooling/imaging and will be discussed in this section; the remaining cavity-related light sources are introduced in chapter 6.

For a discussion of magnetic-optical traps, we refer the reader to the treatment in Ref. [57]. The three important elements for a sizable magneto-optical trap are a high flux of atoms capable of being captured by a MOT (discussed in Sections 2.3 and 2.4), a spherical quadrupole magnetic field (discussed in Section 2.5) and many 10's of mW/cm^2 of $F = 2$ laser light. The effective saturation intensity of the $F = 2 \rightarrow F' = 3$ cycling transition is $I_{sat} = 3.05\,\mathrm{mW/cm^2}$, and to confine a large population several times this value is desirable.

A schematic of the laser system with an accompanying diagram of the relevant atomic structure of rubidium-87 is presented in Figure 2.2. The $F = 2$ slowing laser and the $F = 1$ repump laser are commercial Toptica DL100 ECDL systems with a nominal output power of nominal 50 mW. The diode systems were purported to be self-contained "plug-and-play" units, though we developed several patches to optimize the performance of the lasers. Primarily, patching into the bypass of the electronic control unit was necessary after the Toptica PID controller (PID110) failed to achieve a robust lock. The patch was designed to access the piezoelectric transducer (PZT) which controls the orientation of the external

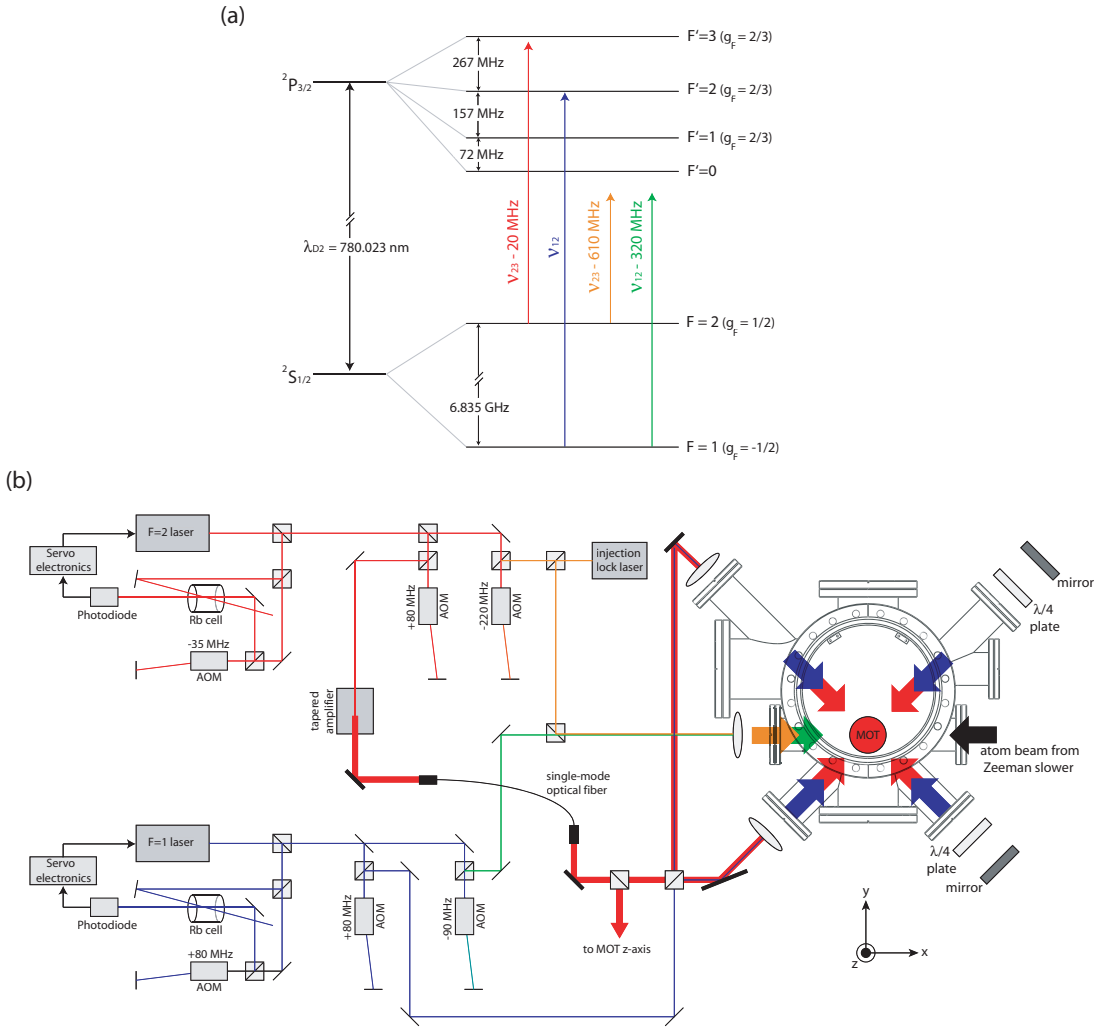

Figure 2.2: The laser-cooling system. (a) Shown are the ground and relevant excited hyperfine states of rubidium-87. (The closely-related D1 transitions – $|^2S_{1/2}\rangle \rightarrow |^2P_{1/2}\rangle$ at $\lambda_{D1} = 795\,\text{nm}$ – are omitted.) Associated with each state is the quantum number F (specified by the eigenvalue equation $(\mathbf{L}+\mathbf{S}+\mathbf{I})^2|F\rangle = F(F+1)\hbar^2|F\rangle$) and, in the limit of a Zeeman shift much less than the hyperfine energy splitting, the "g-factor" for each state (given by the equation $E_B = \mu_B g_F m_z B_z$). The laser frequencies used for the MOT and Zeeman slower are shown on this scale, with false color distinguishing each beam. The optical setup, depicted in (b), shows the crucial laser elements and frequency controls. The two ECDL systems (labeled $F = 2$ and $F = 1$, respectively) are frequency-locked to rubidium vapor cells. The $F = 2$ laser injection locks a 50 mW diode laser to provide the Zeeman slowing light, while the $\sim 200\,\text{mW}$ of MOT light comes from an injection-locked tapered amplifier system which is, in turn, coupled into a single-mode optical fiber. A sketch of the geometric layout of the three beam reflection MOT is shown, relative to the main chamber layout.

grating and thereby the optical feedback. With this control and the current modulation input on the front face of the current control module (DCC110) we were able to utilize home-built PI lockboxes to stabilize the laser frequency. The feedback signal is obtained by frequency modulating the probe beam in the saturation-absorption spectroscopy (SAS) of a rubidium vapor cell. The probe beam is focused onto a photodiode, the output current of which can be mixed down at the modulation frequency to obtain Doppler-free error signals of the hyperfine transitions and their SAS crossover peaks [62]. Activation of the PI lockbox's negative feedback stabilizes the laser frequency to the rubidium reference with a bandwidth of $\sim 1\,\mathrm{MHz}$.

To realize the full laser cooling capabilities of the apparatus, far more than 50 mW of $F = 2$ light is needed to operate a Zeeman slower (Section 2.4) and a MOT well past saturation. After downshifting the $F = 2$ laser frequency by $-610\,\mathrm{MHz}$, a standard master-slave injection lock is established between the locked $F = 2$ and a free-running laser diode, boosting the input slower intensity to 25 mW of laser power[2]. The slower laser beam diameter at the MOT region is $\sim 2.5\,\mathrm{cm}$, yielding a slower saturation parameter of $s = I/I_{sat} \geq 1.7$. The $\geq$ sign is relevant because the slower laser beam converges into the oven region, meaning that the saturation parameter will always exceed 1.7 over the slowing region.

To obtain a large saturation parameter for the MOT as well, an injection-locked tapered amplifier laser diode chip is utilized to boost $\sim 20\,\mathrm{mW}$ of input $F = 2$ laser power to $\sim 350\,\mathrm{mW}$. The mounting and control of the tapered amplifier chip follows that of Ref. [63], with minor design changes for electrical and mechanical isolation. The light produced by the tapered amplifier is then coupled into a single-mode optical fiber, yielding 200 mW of MOT light. As depicted in Figure 2.2, we employed a three-beam retroreflection MOT, which has the advantage of nearly doubling the power per beam. At $\sim 70\,\mathrm{mW}$ per 1 inch diameter laser beam, we obtain a saturation parameter of $s = 4.7$ and ultimately observed MOT populations of ~ 5 billion atoms (as measured by fluorescence [64]).

[2]The free-running laser is capable of 50 mW of output power, but half is lost to the 50-50 beamsplitter which combines the light with the slower repump beam. This intensity cost is required to maintain the proper polarization correlation between the two light fields.

2.3 The Oven

After determining rubidium dispensers to be inadequate for our full experimental requirements [65], we employed a recirculating rubidium oven [66] as the atomic source. The layout of this system is presented in Figure 2.3, which also display the Zeeman slower system that is described in the subsequent section.

The elbow containing the liquid rubidium and the recirculating nozzle have been described elsewhere [63, 66]. The remaining elements of the oven chamber are unique to this experiment however, and deserve mention here. The overarching goal in the construction of the oven chamber was to allow a shuttered atomic beam while minimizing the distance to the entrance of the slower. A custom 6-way cross designed with a minimal length along one axis was employed to accomplish this task. A TEC-cooled two-plate cold catcher was enclosed by the 6-way cross and traps the bulk of the oven-emitted rubidium which does not travel through to the differential pumping tube separating the oven chamber from the Zeeman slower/main chamber region. Between the two cold plates is an aluminum "flag" which acts as a mechanical shutter. The shutter position is controlled by a rotary vacuum feedthrough (Varian L6691-301), rotating the flag into and out of the ballistic path of the atomic beam.

The differential pumping tube is 2.75 inches long with an inner diameter of 5 mm, promising a conductance of 0.2 liters/sec. This allows the oven pressure to exceed 10^{-8} torr with no discernable affect on the main chamber pressure, and the pressure was in the 10^{-9} torr range during normal operation. With the gate valve as the only remaining element separating the oven aperture and the main chamber, the oven-to-slower distance is merely 7.6 inches. The full distance to the MOT center is 42.3 inches.

2.4 Zeeman Slower

The theory behind the functionality of a Zeeman slower is described elsewhere [67, 68, 63]. Briefly stated, an inhomogeneous $B(x)$ is shaped to maintain atomic resonance with a fixed laser slowing beam, despite the ever-reduced Doppler shift of the atoms as they propagate along the x-axis and are slowed from the oven exit velocities of $v \sim 300\,\mathrm{m/s}$ to

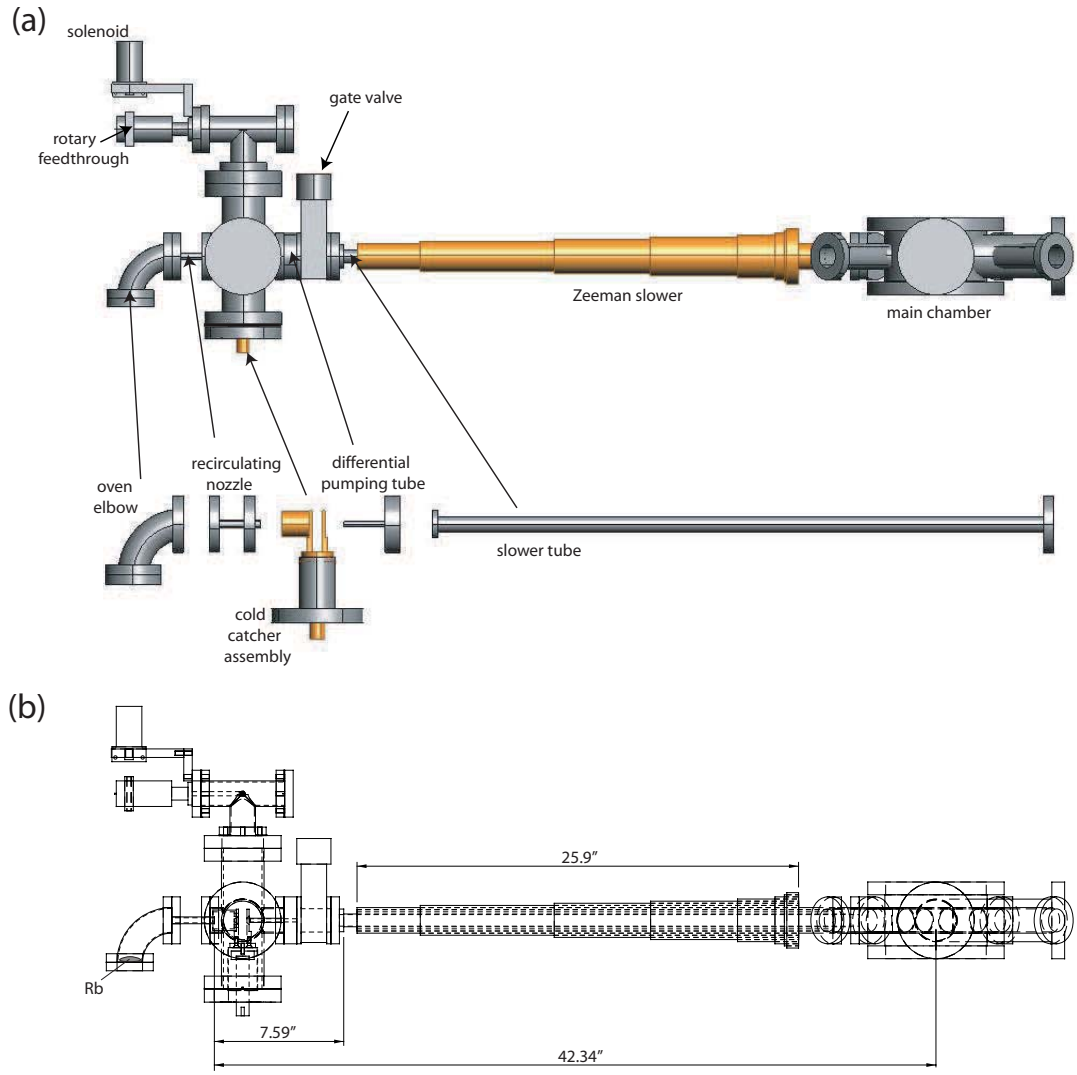

Figure 2.3: Diagram of the skeletal system of the atom delivery systems, the rubidium oven and the Zeeman slower. (a) This diagram shows the critical elements which determine the atomic beam which reaches the main chamber center, 42.3 in. from the oven nozzle opening. (b) Relevant dimensions are shown in this "x-ray" image of the system, including the free propagation distance from oven to Zeeman slower entrance (7.6 in.) and the full slower length (26 in.).

MOT-capturable velocities of $v \lesssim 30\,\mathrm{m/s}$. The maximum deceleration given by dissipative laser cooling is $a_{max} = \hbar k\gamma/2m = 1.15 \times 10^5\,\mathrm{m/s}$, also setting the minimum length $L_{min} = \bar{v}^2/2a_{max} = 0.39\,\mathrm{m}$ of the slower. Given the difficulty in precisely matching the field profile necessary to attain a_{max}, the length of the slower can be increased to yield a uniform deceleration of $a = fa_{max}$. The desired field profile is thus given by

$$B_{slower}(z) = B_v\sqrt{1 - x/L_{slower}} + B_o \tag{2.1}$$

where $B_v \equiv \hbar k\bar{v}/\Delta\mu$, $L_{slower} = L_{max}/f$, and B_o is an arbitrary bias field. The use of a bias field B_o necessitates an accompanied retuning of the slowing laser to $\delta_{slower} = \nu_{laser} - \nu_{eg} = -kv - \Delta\mu B_o$. The layout of the oven and Zeeman slower system is shown in Figure 2.3, and the relevant experimental parameters are summarized in Table 2.2.

Variable	Definition	Value
$\Delta\mu$	magnetic moment difference	$-\mu_B$
$\bar{v}$	avg. entrance atomic velocity	$\sim 300\,\mathrm{m/s}$
B_v	slower capture field	$290\,\mathrm{G}$
v_{cap}	capture velocity	$230\,\mathrm{m/s}$
B_o	bias field	$200\,\mathrm{Gauss}$
δ_{slower}	slower laser detuning	$-610\,\mathrm{MHz}$
f	slower parameter	0.6
a	slower deceleration	$fa_{max} = 6.9 \times 10^4\,\mathrm{m/s}$
L_{slower}	slower length	$L_{max}/f = 0.66\,\mathrm{m}$

Table 2.2: The Zeeman slower parameters for the rubidium $|F = 2, -2\rangle \rightarrow |F' = 3, -3\rangle$ transition. The value of $f = 0.6$ was chosen based on the more sophisticated treatment in Ref. [63].

2.5 Magnetic Trapping and Transfer

The physics of magnetic trapping can be seen directly in the Zeeman energy shifts of the $F = 1$ and $F = 2$ ground states in Figure 2.4. Three of the eight magnetic sublevels $-\{|F = 1, m_F = -1\rangle, |F = 2, m_F = +1\rangle, |F = 2, m_F = +2\rangle\}-$ experience a positive energy shift $\Delta E = g_F m_F \mu_B B$ for an applied field B. In a spatially-inhomogeneous magnetic field $\mathbf{B}(\mathbf{r})$, the force on an atom is given by $\mathbf{F}_B = -g_F m_F \mu_B \nabla|\mathbf{B}(\mathbf{r})|$ and the

aforementioned subset of states are dubbed "weak-field seekers" as the force experienced is along the negative gradient of $|\mathbf{B}(\mathbf{r})|$.

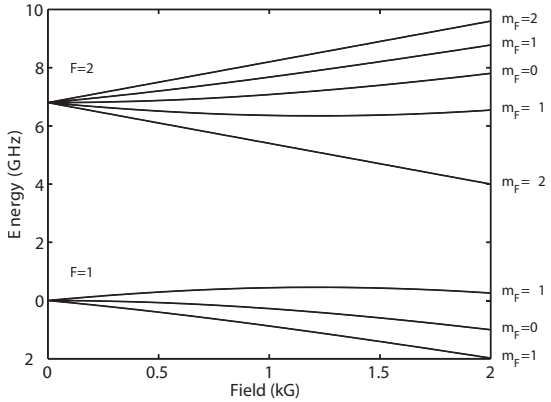

Figure 2.4: Rb-87 Zeeman splitting for hyperfine ground states

Maxwell's equations in free space require $\nabla \cdot \mathbf{B}(\mathbf{r}) = 0$ and $\nabla \times \mathbf{B}(\mathbf{r}) = 0$. If $\mathbf{B}(\mathbf{r})$ has a minimum at $\mathbf{r} = 0$, then Taylor expansion of the field is

$$\mathbf{B}(\mathbf{r}) = \mathbf{B}(\mathbf{r}=0) + [(\mathbf{r}\cdot\nabla)\mathbf{B}]_{\mathbf{r}=0} + \frac{1}{2}\left[(\mathbf{r}\cdot\nabla)^2\mathbf{B}\right]_{\mathbf{r}=0} + \mathcal{O}(r^3). \tag{2.2}$$

The magnetic trapping of atoms is achieved for weak-field seeking atoms orbiting about a magnetic field minimum. There is a class of magnetic field arrangements which are prevalent in atom trapping [20, 69], four of which were employed in this thesis. We begin with the simplest configuration, the spherical quadrupole trap, and will introduce the remaining trapping configurations in chapters 2 and 3 in the context of the millitrap.

2.5.1 Spherical Quadrupole Trap

Considering the specific case of Equation (2.2) where $\mathbf{B}(0) = 0$, the lowest order expansion of the field is given by

$$\mathbf{B}(\mathbf{r}) = [(\mathbf{r}\cdot\nabla)\mathbf{B}]_{\mathbf{r}=0} + \mathcal{O}(r^2). \tag{2.3}$$

This is a generalized quadrupole field, so named because two magnetic dipoles are required to obtain zero field at a specific location or, equivalently, because the field looks quadrupolar, i.e. $B(r,\theta) \propto 1/r^4$ for large r. A *spherical* quadrupole field is obtained in the case of

cylindrical symmetry, i.e. the coils which produce the field are co-axial. The lowest-order field profile is specified by a single gradient B':

$$\mathbf{B}(\mathbf{r}) = B'\,(x, y, -2z)\,. \tag{2.4}$$

This can be achieved by two identical coils of radius R, separated by distance $2d$, carrying current I_c in opposite directions. At the center of the coils, the field is that of Equation (2.4) with $B' = 6\mu_o I_c R^2/(d^2 + R^2)^{5/2}$.

A magneto-optical trap which collects and cools the initial gaseous sample requires just such a spherical quadrupole field and appropriate laser-cooling light [57, 70]. To trap the cold atomic sample for delivery to the millitrap/cavity region, the same coils which form the fields necessary for the MOT can be employed to form a spherical quadrupole trap. It is important to mention at this point that, first and foremost, a magnetic trap on Earth must support the atoms against gravity. Incorporating gravitational energy, the potential seen by a ^{87}Rb atom in a spherical quadrupole trap is given by

$$U = mgz + g_F m_F \mu_B B' \sqrt{x^2 + y^2 + 4z^2}, \tag{2.5}$$

where $g = 9.8\,\mathrm{m/s^2}$, the gravitational acceleration at the earth's surface. To trap against this force, a minimum gradient of $B'_{min} = mg/2g_F m_F \mu_B$ is required, and realizing a B' significantly larger than B'_{min} is desirable to prevent significant vertical asymmetry in the trap. For $|F = 1, m_F = -1\rangle$ ^{87}Rb atoms, $B'_{min} = 31\,\mathrm{G/cm}$.

2.5.2 Quadrupole Transfer System

Greiner *et al.* [71] developed an elegant method to transport atoms trapped in spherical quadrupole traps. To transfer the atoms from one location to another, the cylindrical symmetry of a single quadrupole trap is broken with the addition of a second quadrupole coil pair with its balanced trap center in the same $x-y$ plane as the first coil pair. Without loss of generality, the center of the second coil pair is placed at $(0, y_o, 0)$. Powering both coils with currents I_1 and I_2, respectively, leads to superposed spherical quadrupole fields. These coils can have distinct geometries, i.e. different radii $R_{1,2}$ and coil separations $2d_{1,2}$, leading to differing gradient/current ratios. If $y_o \leq R_1 + R_2$, then the field vanishes in only

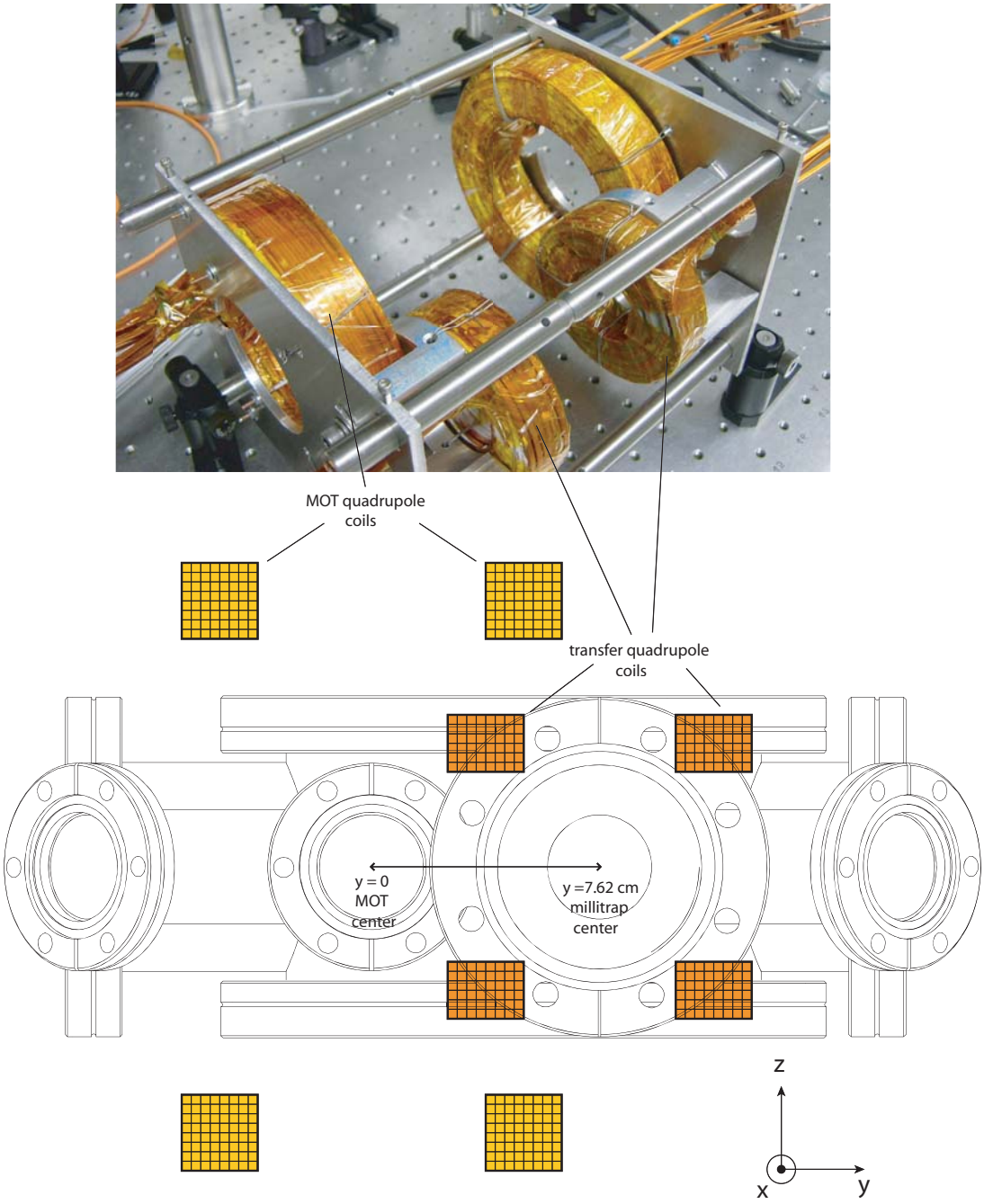

Figure 2.5: Magnetic quadrupole transfer system. A side view of the chamber is overlaid for perspective.

one location and, as the ratio of coil currents I_1/I_2 is varied from 0 to ∞, the location of this field zero is mapped from $y = 0$ to $y = y_o$.

This is precisely the process by which magnetically trapped atoms, loaded in the MOT region, are moved to the millitrap/cavity region. The size and shape of the two spherical quadrupole coil pairs are constrained by the physical dimensions of the vacuum chamber. The coil pairs were dubbed the "MOT quadrupole coils" and the "cavity quadrupole coils," respectively, with latter so named because they were coaxial with the high-finesse cavity that was ultimately installed in the chamber (described in chapter 6). A reentrant "bucket"[3] is utilized to minimize the coil separation of the transfer coils, but the MOT quadrupole coils are forced to a front-face separation of 6 inches. The relevant physical dimensions of the coils are presented in Table 2.3.

Coil Pair	y_o	**ID**	**OD**	d_{front}	d_{back}	**No. of turns**	B'/Amp
MOT coils	0	3 in.	5 in.	3 in.	4 in.	8×8	0.25 G/cm/A
Transfer coils	3 in.	2 in.	4 in.	1.5 in.	2.25 in.	8×6	0.55 G/cm/A

Table 2.3: Magnetic transfer coil parameters.

Despite the many turns of wire which make up the two coil pairs, the relatively low B'/Amp ratios requires large currents to exceed B'_{min}. Experimentally, hundreds of Amps are needed for optimal performance, necessitating large current power supplies and water-cooled wire (Kapton-insulated, square $\frac{1}{8}" \times \frac{1}{8}"$ hollow copper wire). A 300 psi high-pressure water pump (300 psi) flows water through the MOT and cavity coil assemblies, broken up into 2×8 turns to maintain sufficient water flow. The Joule heating generated during the $20 - 30$ seconds of magnetic trapping and transfer is sizeable, and Kater's interlock system would interrupt the supply current if either the water temperature or flow rate fell outside of their normal operational tolerances.

The gradient fields and trap positions are presented in Table 2.5.2, with the information organized in a matrix such that each cell gives the quadrupole field parameters for given coil currents.

[3]The "bucket" moniker is applied because the element consists of an 8" conflat flange welded to a recessed steel platform which extends 0.75" past the flange face into the chamber. See Appendix B for engineering drawings.

KEY	I_{CQ}
I_{MOT}	y_o (cm) dB/dy (G/cm) dB/dx (G/cm) -dB/dz (G/cm)

	0 **A**	40 **A**	80 **A**	120 **A**	160 **A**	200 **A**	240 **A**	280 **A**	320 **A**	360 **A**	400 **A**
		7.62	7.62	7.62	7.62	7.62	7.62	7.62	7.62	7.62	7.62
0		22.6	45.3	67.9	90.6	113.2	135.9	158.5	181.2	203.8	226.5
A		22.6	45.3	67.9	90.6	113.2	135.9	158.5	181.2	203.8	226.5
		45.3	90.6	135.9	181.2	226.5	271.8	317.1	362.4	407.7	453.0
	0.0	5.52	6.67	7.00	7.16	7.26	7.32	7.36	7.40	7.42	7.44
40	10.3	15.0	40.8	64.3	87.4	110.3	133.1	155.8	178.6	201.3	224.0
A	10.3	26.7	50.2	73.0	95.7	118.4	141.1	163.7	186.4	209.1	231.7
	20.6	41.8	90.7	137.3	183.1	228.7	274.1	319.6	365.0	410.3	455.7
	0.0	1.78	5.52	6.32	6.67	6.87	7.00	7.10	7.16	7.22	7.26
80	20.7	9.8	30.1	57.1	81.6	105.3	128.6	151.8	174.8	197.7	220.5
A	20.7	26.1	53.4	77.3	100.3	123.2	146.0	168.7	194.4	214.1	236.8
	41.1	36.0	83.5	134.4	181.9	228.5	274.6	320.5	366.2	411.8	457.3
	0.0	0.92	3.64	5.52	6.14	6.47	6.67	6.82	6.92	7.00	7.07
120	31.0	22.1	12.3	45.1	72.8	98.1	122.4	146.2	170.0	192.9	216.1
A	31.0	35.0	51.6	80.1	104.2	127.5	150.5	173.4	196.2	218.9	214.7
	62.1	57.1	63.9	125.3	177.0	225.6	272.9	319.6	365.8	411.9	457.8
	0.0	0.63	1.77	4.43	5.52	6.02	6.32	6.53	6.67	6.79	6.87
160	41.4	33.2	19.7	27.3	60.2	88.3	114.2	139.0	163.2	187.0	210.6
A	41.4	45.0	52.3	79.9	106.9	131.1	154.5	177.7	200.7	223.5	246.4
	82.7	78.2	71.9	107.2	167.0	219.4	268.7	316.7	363.9	410.6	457.0
	0.0	0.48	1.20	2.76	4.74	5.52	5.94	6.22	6.41	6.56	6.64
200	51.7	43.9	32.5	17.1	43.0	75.2	103.6	130.0	155.3	179.9	204.0
A	51.7	55.1	60.5	75.0	107.2	133.6	157.9	181.5	204.8	227.9	250.8
	103.5	99.0	93.0	92.1	150.2	208.8	261.5	311.5	360.0	407.7	454.8
	0.0	0.39	0.92	1.77	3.64	4.92	5.52	5.88	6.14	6.32	6.47
240	62.1	54.5	44.2	29.5	24.6	58.5	90.3	118.9	145.6	171.3	196.2
A	62.1	65.4	70.0	78.4	103.3	134.3	160.3	184.7	208.4	231.8	255.0
	124.2	119.9	114.3	107.9	127.9	192.7	250.6	303.6	354.0	403.0	451.2
	0.0	0.33	0.75	1.34	2.42	4.14	5.03	5.52	5.84	6.07	6.24
280	72.4	65.0	55.5	42.6	26.0	39.0	73.8	105.3	135.1	161.1	187.1
A	72.4	75.6	79.9	86.3	99.9	131.8	161.2	187.0	211.5	235.3	258.8
	144.9	140.7	135.4	128.9	125.9	170.8	235.0	292.3	345.5	396.4	445.9
	0.0	0.28	0.63	1.09	1.78	3.09	4.43	5.10	5.52	5.81	6.02
320	82.8	75.5	66.4	54.8	39.3	27.3	54.6	89.7	120.3	149.2	176.5
A	82.8	85.9	89.9	95.4	104.6	126.1	159.7	188.0	213.7	238.3	262.2
	165.6	161.4	156.3	150.2	143.9	153.4	214.3	277.1	334.1	387.5	438.7

Table 2.4: The table of positions and field gradients for the magnetic transfer system. The cylindrical symmetry is of course broken with two quadrupole coil pairs, so with both sets running current the three cartesian gradients are unequal about the field zero. Three typical experimental configurations (the latter two of which are explained in chapter 3) are the following:

MOT loading : $I_{MOT} = 75\,\mathrm{A}$, $I_{CQ} = 0$, $y = 0$, $B' = 18.1\,\mathrm{G/cm}$

Quadrupole evaporation : $I_{MOT} = 200\,\mathrm{A}$, $I_{CQ} = 240\,\mathrm{A}$, $y = 5.94\,\mathrm{cm}$,
$\nabla|\mathbf{B}| = (104\,\mathrm{G/cm},\ 158\,\mathrm{G/cm},\ -262\,\mathrm{G/cm})$

Millitrap handoff : $I_{MOT} = 0$, $I_{CQ} = 240\,\mathrm{A}$, $y = 7.62\,\mathrm{cm}$, $B' = 136\,\mathrm{G/cm}$

2.6 Imaging

With the atoms being formed in the loading region and then transported to the millitrap/cavity region, diagnostic imaging is possible at several chamber locations. Table 2.5

summarizes the physical apertures constraining the imaging system, though typically the image quality is experimentally limited by the optics and CCD camera pixelation (Roper Scientific Photometrics CoolSNAP ES, 6.5 μm×6.5 μm pixel size).

Imaging location	**NA**
MOT region (top)	0.16
Outside millitrap (side)	0.19
Inside millitrap (top)	0.16
Inside millitrap (top, 40 ms TOF)	0.11
Inside millitrap (side)	0.10
Inside cavity (side)	0.10

Table 2.5: Limiting numerical apertures for the imaging system.

2.7 The Full Cooling Apparatus

With all of the elements presented in the preceding sections, the full system is depicted in Figure A. The figure also shows the integration of two elements, namely the millitrap electrical feedthrough port and the liquid nitrogen feedthrough, both of which will be described in the next chapter. Finally, a recent picture of the experiment (shown in Figure 2.7) obscures the elements discussed in this chapter, but shows the substantial infrastructure in which the system resides.

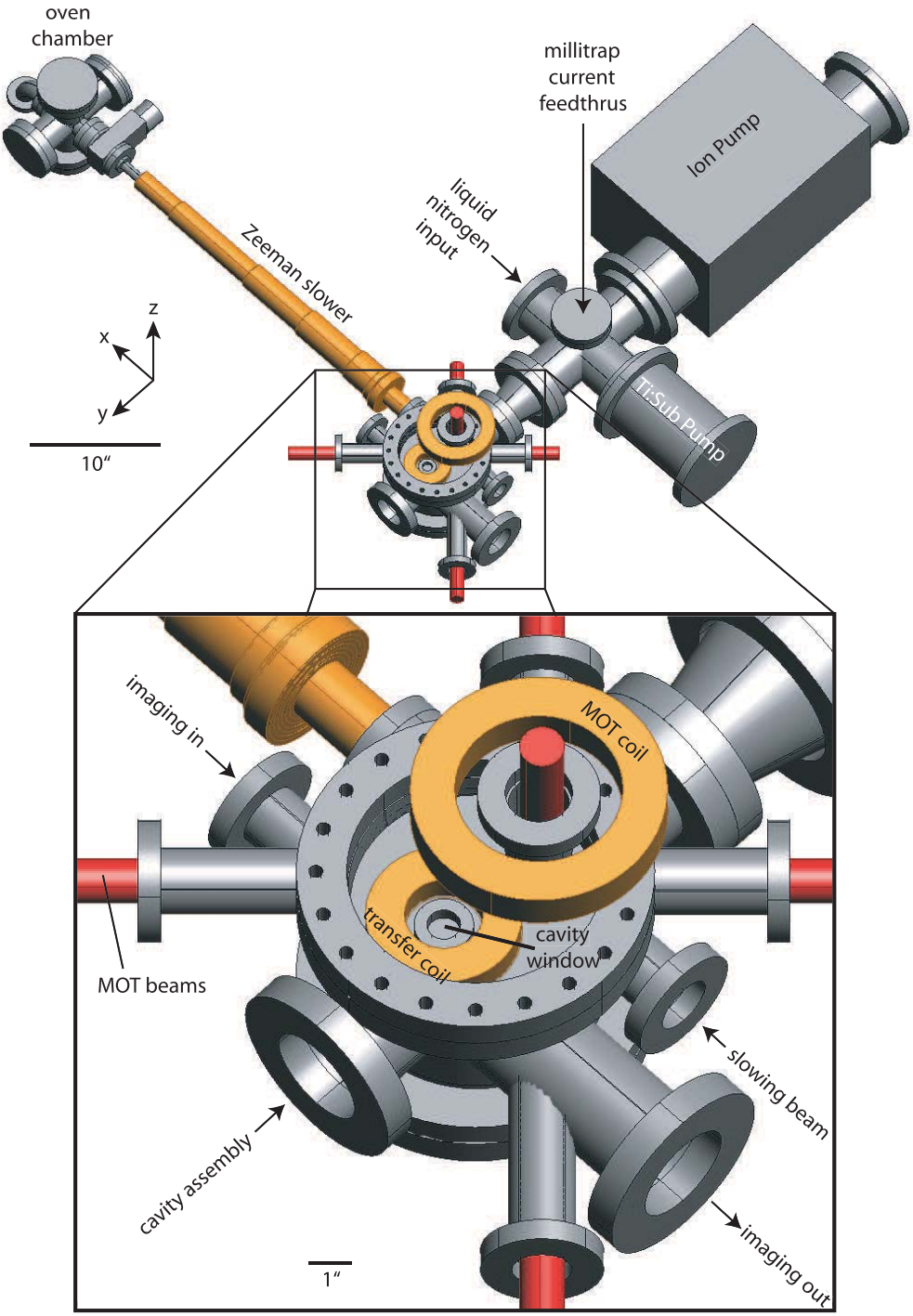

Figure 2.6: The full vacuum chamber layout.

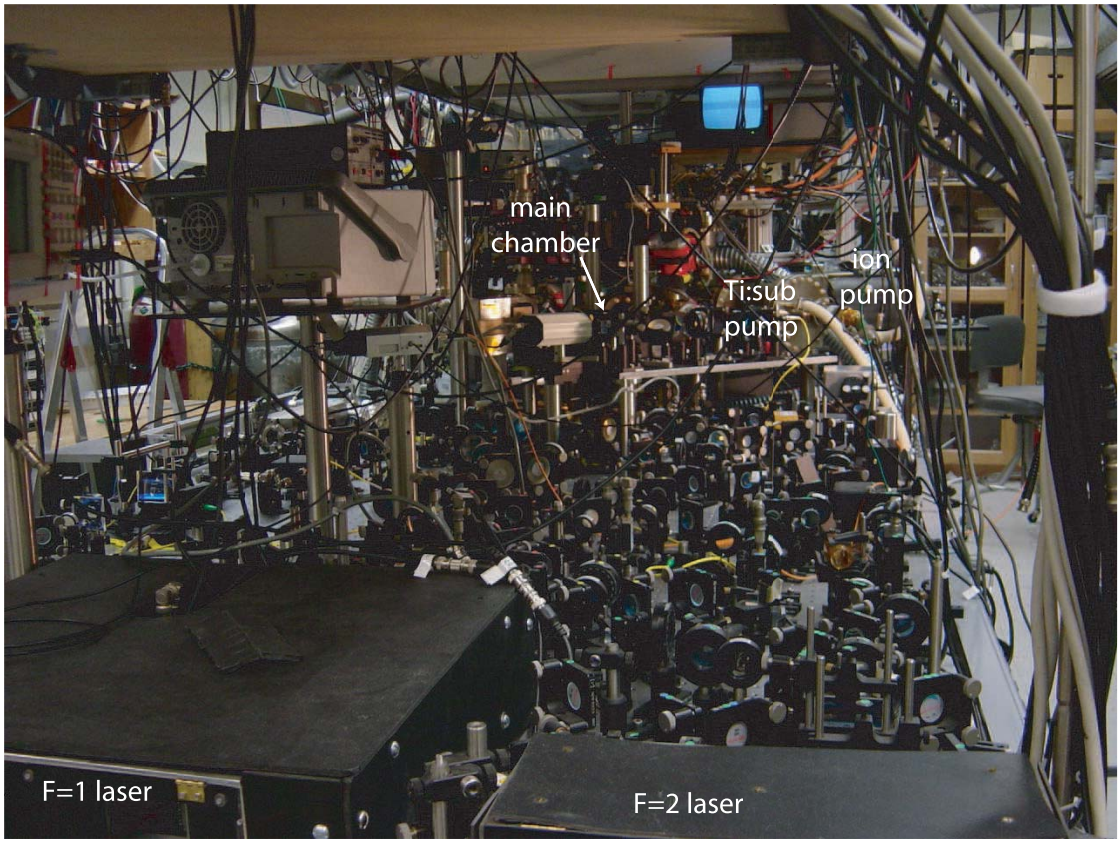

Figure 2.7: Photo of the experiment.